

RSC Advances



This is an *Accepted Manuscript*, which has been through the Royal Society of Chemistry peer review process and has been accepted for publication.

Accepted Manuscripts are published online shortly after acceptance, before technical editing, formatting and proof reading. Using this free service, authors can make their results available to the community, in citable form, before we publish the edited article. This *Accepted Manuscript* will be replaced by the edited, formatted and paginated article as soon as this is available.

You can find more information about *Accepted Manuscripts* in the [Information for Authors](#).

Please note that technical editing may introduce minor changes to the text and/or graphics, which may alter content. The journal's standard [Terms & Conditions](#) and the [Ethical guidelines](#) still apply. In no event shall the Royal Society of Chemistry be held responsible for any errors or omissions in this *Accepted Manuscript* or any consequences arising from the use of any information it contains.

Improved supercapacitive charge storage in electrospun niobium doped titania nanowires

Baiju Vidyadharan,¹ Panikar Sathyaseelan Archana,² Jamil Ismail,¹ Mashitah M. Yusoff,¹ and Rajan Jose^{1*}

¹ Nanostructured Renewable Energy Materials Laboratory, Faculty of Industrial Sciences & Technology, Universiti Malaysia Pahang, 26300 Kuantan, Malaysia; ² Department of Chemistry, University of Alabama, 250 Hackberry Lane, Shelby hall, Tuscaloosa 35401, Alabama, USA; * corresponding author: rjose@ump.edu.my/ joserajan@gmail.com

Abstract

Supercapacitors are emerging as a desirable energy storage medium in view of their order of magnitude higher power density than batteries and energy density than electronic capacitors. One of the key issues in the development of a suitable electrode material for supercapacitors is that materials showing large specific capacitance are poorly abundant. In this paper, we show that niobium doped titanium dioxide (Nb:TiO₂) nanowires developed by electrospinning have an order of magnitude higher capacitance (~280 Fg⁻¹) than pristine TiO₂ (~40 Fg⁻¹) or zirconium doped TiO₂ (~30 Fg⁻¹). The cyclic voltammetry and charge discharge cycling experiments show that the Nb:TiO₂ nanowires have 100% coulombic efficiency and could be operated over 5000 cycles without any appreciable capacitance degradation. The superior charge storage capability of the Nb:TiO₂ is assigned to its high electrical conductivity as determined by electrochemical impedance spectroscopy. A practical supercapacitor is fabricated in asymmetric configuration using the Nb:TiO₂ as anode and activated carbon as cathode. The device delivered energy densities of 16.3, 11.4 and 5.6 Whkg⁻¹ at power densities of 770, 1310, and 1900 Wkg⁻¹, respectively. These values are much superior than a control device fabricated using activated carbon as its both electrodes.

Keywords: Asymmetric Supercapacitor, Ceramic nanostructures, Renewable energy, Batteries, TiO₂ nanostructures, One-dimensional nanostructures.

Introduction

Energy storage devices providing high energy and power density are required to meet the ever increasing demands to power hybrid electric vehicles and multifunctional portable electronic devices.¹⁻³ Practical energizers, such as lithium ion batteries, have high energy density ($>150 \text{ Whkg}^{-1}$) but suffer from low power density ($< 200 \text{ Wkg}^{-1}$) and short cycle life (<1000 cycles).⁴ On the other hand, conventional capacitors have three orders of magnitude higher power density ($>10^5 \text{ Wkg}^{-1}$) but low energy density ($< 5 \text{ Whkg}^{-1}$) than batteries. Electrochemical capacitors or supercapacitors (SCs), with orders of magnitude higher power density ($>10 \text{ kWkg}^{-1}$) than batteries and energy density ($\sim 50 \text{ Whkg}^{-1}$) than capacitors, can bridge the gap between the batteries and conventional capacitors. The SCs are classified into electric double layer capacitors (EDLCs) and pseudocapacitors according to the charge storage mechanisms. The EDLCs store electrical energy via accumulation of electric charges at an electrical double layer formed at an interface between a porous solid electrode and an electrolyte (non-faradic). Carbons such as activated carbon, carbon nanotubes, and graphene are choices to build EDLCs; however, their lower specific capacitance ($C_S \sim 20 - 50 \text{ } \mu\text{Fcm}^{-2}$) limit their application areas. The pseudocapacitors provide several times higher C_S (10 – 100) than EDLC due to faradic charge storage process facilitated by a redox reaction at the electrode – electrolyte interface.^{5,6} Transition metal oxides (TMOs), such as MnO₂, Co₃O₄, RuO₂, and conducting polymers show high pseudocapacitance (C_P); a theoretical C_P equal to $nF / (\Delta E \times m)$, where F is the Faraday constant, n is the number of electrons transferred, m is the molecular weight and ΔE is the redox potential of the material, could be achieved by these materials.⁷ Although the potential window of the pseudocapacitive materials are lower

compared to that of the carbons they are employed in the SCs as one of the electrodes to enhance the energy density. Such device configuration is termed as asymmetric supercapacitors (ASCs). Even if the intense research on SCs is aimed at increasing energy density similar to that of batteries, attention is equally given at lowering fabrication costs and on materials of larger abundance.

High electrochemical reversibility, multiple oxidation states, large surface area, and high electrical conductivity are properties required for high performance SC electrodes. Among the TMOs, TiO₂ have relatively lower toxicity, larger abundance and lower cost, environmental friendly, and desirable optical, electrical and electrochemical properties.⁸ It has been extensively studied for its wide application from catalysis to energy storage.^{9,10} For its application in SCs, theoretically TiO₂ could deliver specific capacitance 700 Fg⁻¹ (See Electronic Supplementary Information,† ESI,† S1); i.e., TiO₂ nanostructures hold good promise as a desirable SC electrode. However, its practically achieved C_S is rather low thereby limiting its commercial deployability (see Table 2). We believe that this poor performance could be related to the inferior electrical conductivity of nanostructured TiO₂ (~10⁻⁵ S/cm)^{11,12}. Doping of TiO₂ with transition metals such as W⁺⁶, Nb⁺⁵, V⁺⁵, Ce⁺⁴, Zr⁺⁴, Fe⁺³ and Ni⁺³ or non-metals such as H and N is considered to be one of the efficient method to improve the electrical conductivity of TiO₂.¹³⁻¹⁶ The Nb doped TiO₂ (Nb:TiO₂) have three orders of magnitude higher electrical conductivity than pristine TiO₂^{11,17} and show superior performance in electrochemical devices.

One-dimensional charge transport makes nanowires to be preferred charge storage medium. Among the many nanowire forming techniques, electrospinning is a simple and versatile technique for continuous nanofibers and nanowires for many applications such as filtration, healthcare, and energy.¹⁸ In the electrospinning technique, a polymeric solution,

usually prepared in organic solvents, is injected through a syringe needle in the presence of an electric field. A polymeric jet is initiated upon injection of the solution that undergoes asymmetric bending during the passage between the injector and the collector. This asymmetric bending increases the path length of the jet and allows the solvent to evaporate thereby producing solid continuous fibers with diameters ranging from nanometers to sub-micrometers on a collector surface. If the polymeric solution contains precursors for forming an inorganic solid, then appropriate annealing produces its continuous nanofibers.

In this work, we show that electrospun Nb:TiO₂ nanowire electrodes display an order of magnitude higher specific capacitance (~280 Fg⁻¹) and superior electrochemical reversibility (100% at the end of 5000 cycles) in 3 M KOH electrolyte than pristine TiO₂ or Zr:TiO₂. A working SC in asymmetric configuration was fabricated using Nb:TiO₂ as anode and commercial activated carbon as cathode which gave the highest energy density (E_S) that employed TiO₂ nanostructures. The performance of the asymmetric supercapacitor (ASC) is four times higher than a control device, which is a symmetric EDLC fabricated using activated carbon (AC). The ASC could be cycled over 5000 times in the voltage window 0-1.5 V with no appreciable capacitance loss. Our results demonstrate that the electrospun Nb:TiO₂ nanowires could be a choice of SC electrode material characterized by high C_S and related properties.

2. Experimental Details

2.1 Synthesis and characterization of TiO₂, Nb:TiO₂, and Zr:TiO₂ nanowires

In a typical synthesis, TiO₂, Nb:TiO₂, Zr:TiO₂ nanowires were prepared by a commercial electrospinning machine (Electroris, Nanolab, Malaysia) using a previously adopted procedure.^{16,14,19} The niobium is doped up to 5 at.% and zirconium up to 2at.% as the niobium doping showed improved performance than the parent material. The precursor

solution for electrospinning was prepared from polyvinyl acetate (PVAc, Mw 500000), dimethyl formamide (DMF), titanium (IV) isopropoxide, niobium ethoxide (Sigma Aldrich, Singapore; 99.9%), zirconyl chloride, and acetic acid. In a typical synthesis, 4.5 g of PVAc solution in DMF (11.5 wt.%) was mixed together with titanium (IV) isopropoxide. The amounts of Ti and Nb /Zr precursors required were calculated based on the number of atoms required for replacing a given number of Ti atoms by Nb or Zr atoms. A sol was prepared by the drop wise addition of 0.5 g of acetic acid to the above solution. The resulting solution was stirred well and electrospun at 25 kV accelerating voltage and at 1 mLh⁻¹ flow rate. The polymeric fibers containing Ti⁴⁺ and Nb⁵⁺/Zr⁴⁺ ions were collected on a grounded rotating drum placed at 10 cm below the spinneret.

The morphology of the as-spun and annealed nanowires were examined by scanning electron microscopy (SEM; Quanta 200 FEG System: FEI Company, Oregon) and transmission electron microscopy (TEM; JEOL 2010Fas, Tokyo, Japan). Crystal structure of the nanowires was examined by XRD (Siemens D5005, Bruker, Karlsruhe, Germany) technique. Presence of Nb and Zr in the doped materials was confirmed by X-ray fluorescence measurements employing EDX-720 (Shimadzu).

2.2 Electrode preparation and electrochemical studies

Supercapacitor electrodes were fabricated on nickel foam substrates as described before.²⁰ Briefly, the working electrode was prepared by mixing the nanowires with polyvinylidene fluoride (PVDF) (Sigma Aldrich, USA) and carbon black (Super P conductive, Alfa Aesar, UK) in the ratio 75:15:10. The above mixture was stirred in N-methyl-2-pyrrolidinone for better homogeneity. The as-prepared slurry was then pasted on a nickel foam substrate (area ~1 cm²) and dried in an oven at 60 °C for 24 h. The mass loading of active material was ~ 2.5 mgcm⁻². The dried electrode was then pressed using a hydraulic

press at a pressure of 5 ton. Electrochemical properties of the electrodes were studied by cyclic voltammetry (CV), galvanostatic charge–discharge cycling, and electrochemical impedance spectroscopy in 3 M KOH electrolyte. These electrochemical properties in three electrode configurations were obtained at room temperature using a potentiostat galvanostat (PGSTAT M101, Metrohm Autolab B.V., Netherlands) employing NOVA 1.9 software. A platinum rod and a saturated Ag/AgCl electrode were used as the counter and the reference electrodes, respectively.

2.3 Asymmetric supercapacitor fabrication and testing

The ASCs were fabricated by assembling the Nb:TiO₂ nanowire (anode) and the AC (cathode) electrodes separated by a glass microfiber filter (fioroni) in 3 M KOH. The amount of active materials for fabrication of ASC was calculated based on the charge balance between the electrodes such that the effective capacitance at each electrode is same (See Results and Discussion section for details). A symmetric EDLC comprising of AC as both electrodes was used a control device. The capacitive properties of the ASC were obtained in two-electrode configuration at room temperature using the PGSTAT M101 potentiostat-galvanostat.

3. Result and Discussion

3.1 Morphology and Crystal structure of electrospun nanowires

Fig. 1 shows the crystal structure of pristine and doped TiO₂; all materials crystallized in anatase structure. The XRD peaks of the doped materials showed either a shift in the peak positions or change its profile (Inset of Fig. 1). The doping has been confirmed by chemical analysis employing X-ray fluorescence measurements (See ESI,† S2). The crystallinity of the doped materials, which was judged from the *fwhm* of the XRD peaks, was appreciably

different for the Nb and Zr doped analogues (Inset of Figure 1). The Zr:TiO₂ showed broader and diffused peaks than pure and Nb:TiO₂, which could be due to increased lattice strain.^{14,16} The lattice parameters of the materials calculated using the procedure described elsewhere^{14,16} from the XRD patterns are summarized in Table 1. The lattice parameters of the TiO₂ and the doped materials agree well with reported values.^{14,16} Table 1 shows that Nb decrease *a* whereas Zr decrease both *a* and *c* of the unit cell of anatase TiO₂. This difference is expected to originate from the difference in the sizes of the six-fold coordinated (which is the geometry in the anatase TiO₂) Ti⁴⁺ (0.605 Å), Nb⁵⁺ (0.64 Å), and Zr⁴⁺ (0.72 Å). The larger size of the six-fold coordinated Zr⁴⁺ ions could influence the lattice structure of anatase more than the Nb⁵⁺ with minor mismatch.

Morphological and microstructural details of doped and undoped TiO₂ nanowires are summarised in Fig. 2. The as-spun mats showed conventional electrospun polymeric fibrous structure which upon annealing produced the targeted metal oxide structures with their diameter in the range 100 – 150 nm. The TEM images showed lowering of grain size with doping for all the dopants. The undoped TiO₂ fibres had grains of larger diameter (~ 50 nm). The doped fibres were constituted by grains of lower diameter (~ 10-30 nm) implying that the doping reduced the grain growth under similar processing conditions.

3.2 Cyclic voltammetry

Cyclic voltammetry measurements were performed to evaluate the electrochemical behavior of the electrodes under a potential window 0 – 0.5 V. Figure 3a shows the CV curves of the electrodes of pristine TiO₂, Zr:TiO₂ and Nb:TiO₂ measured at a scan rate 2 mVs⁻¹ in 3 M KOH aqueous electrolyte. In the CV plot of the electrodes, a pair of redox peaks are seen which indicate that the origin of charge storage is reversible faradic process. These

peaks can be attributed to the insertion/exertion of alkali cations into/out of the oxide nanowires with concomitant reduction/oxidation of the Ti ions, which can be expressed as



A high voltametric current (4 mA) is generated from 2at.%Nb:TiO₂ against <1 mA from pristine TiO₂ at 2 mVs⁻¹ scan rate. It could be attributed to the enhanced faradic reaction due to the improved electrical conductivity of the Nb:TiO₂. However, the voltammetric current in the 5at.% Nb:TiO₂ dropped to ~50% (~2 mA) of that in 2at.% Nb:TiO₂ (4 mA), which most likely arise from the increased crystal defects in this sample and consequent charge trapping.¹⁶ On the other hand, a much larger drop was observed in the voltametric current generated from Zr:TiO₂. The difference in anodic peak potential (E_A) and cathodic peak potential (E_C) is a measure of reversibility and internal resistance of the material.²¹ The difference in potential ($E_C - E_A$) is found to be ~ 61 mV, 62 mV and 59 mV for pristine TiO₂, Zr:TiO₂, and Nb: TiO₂ respectively at 2 mVs⁻¹. The smaller value of ($E_C - E_A$) of Nb:TiO₂ indicates that the electrode material is highly reversible and has low internal resistance.²² The ratio of area of the cathodic scan to that of anodic scan is a measure of coulombic efficiency and is found to be 93, 91, and 100% for pristine TiO₂, Zr:TiO₂ and 2at.% Nb:TiO₂, respectively. However, the coulombic efficiency reduced to 89% for 5at.% Nb:TiO₂.

Fig. 3(b-d) shows the CV curves of all electrodes at different scan rate from 2 – 60 mVs⁻¹. Because the 5at.% Nb:TiO₂ showed inferior performance than its 2at.% counterpart, details of its CV analysis is given in the ESI† (S3). The CV of the is in The CV profiles show oxidation (anodic) and reduction (cathodic) events at all scan rate, which are characteristics of pseudocapacitance. The anodic peak in the CV profile shifted towards positive potentials with increase in the scan rate and the cathodic peak to the negative potential on account of the polarization in the electrode material. The asymmetric and scan

rate dependent shape of the CV profiles show that the origin of the capacitance is by fast and reversible faradic reaction. The C_S (Fg^{-1}) of the samples was estimated from the cathodic or anodic part of the CV data using the equation:

$$C_S = \frac{1}{mv(E_2 - E_1)} \int_{E_1}^{E_2} i(E) dE \quad (2)$$

where E_1 and E_2 are the cutoff potentials in the CV curves and $i(E)$ is the current at each potential, $E_2 - E_1$ is the potential window, m is the mass of the active material, and v is the scan rate. Fig. 4a shows the variation of C_S with scan rate of all electrode materials. Slower scan rates enable higher diffusion of alkali cations into the nanowire electrodes thereby accessing a major fraction of the active site in the material and show high C_S . This makes 2 at.% Nb:TiO₂ active material for potential energy storage application.

In pseudocapacitive materials, scan rate (v) dependence of voltammetric current (I) is analyzed to determine whether the capacitance originates from surface redox reaction or from bulk diffusion. $I \propto v$ surface redox reaction and $I \propto \sqrt{v}$ for semi-infinite bulk diffusion. We observed a straight line for $i \propto \sqrt{v}$ (Fig. 4b&c); therefore, bulk redox reaction occurred during the electrochemical reaction for both pristine TiO₂ and Nb:TiO₂, which is expected to be the source of the observed larger capacitance. But a straight line is observed for $I \propto v$ in case of Zr:TiO₂ (Fig. 4d) which indicate that Faradic charge storage is limited only on the surface of the material. In case of semi- infinite diffusion, I can be expressed by the Randle's -Sevcik equation at 25 °C, ^{23,24}

$$I = 2.69 \times 10^5 \times n^{3/2} \times D^{1/2} \times A \times C_0 \times \sqrt{v} \quad (3)$$

where n is the number of electron transferred, A is the surface area of the electrode, D is the diffusion coefficient, v is the scan rate, and C_0 is the initial ion concentration. Based on slope

of I vs \sqrt{v} graph and Eq (3), diffusion coefficients of the electrolyte ions for the 2at.% Nb:TiO₂ and pristine TiO₂ electrode are found to be 1.08×10^{-13} and 9.16×10^{-15} cm²s⁻¹, respectively (see ESI,† S4); i.e., the Nb:TiO₂ offers two order of magnitude higher ion diffusivity than pristine TiO₂. The observed ion diffusivity for Nb:TiO₂ among the highest values reported for supercapacitor electrode materials.^{25,24}

To isolate the supercapacitive performance of the active materials from the Ni foam substrate, the background capacitance of Ni foam was evaluated from the area under the CV curve. The area of the CV curve without using the active materials was $\sim 1.3 \times 10^{-4}$, which is only ~ 0.01 % of the total area in the presence of it (See ESI,† S5), thereby suggesting that contribution from the Ni foam is negligible in our experiment.

3.3 Galvanostatic Charge- discharge study

Fig. 5a shows the discharge curves for the pristine and doped nanowire electrodes in 3 M KOH aqueous electrolyte at a discharge current density 1 Ag^{-1} in the voltage range of 0–0.5 V. The longer discharge duration of the Nb:TiO₂ electrodes as compared to the other ones at the similar current density shows the enhanced pseudocapacitance of the Nb:TiO₂ electrodes. The potential drop during the discharge process, generally caused by the internal resistance (R) and incomplete faradic reaction of the device, was rather low (~ 14.8 mV) for Nb:TiO₂ nanowire electrodes. This lowering of R (see ESI,† S6) could be attributed not only due to the high electrical conductivity offered by donor impurity and also due to the one-dimensional nature of the electrode material (Fig. 2).

Fig. 5b shows the rate dependent discharge profile for the Nb:TiO₂ electrode in the potential window 0-0.5 V in 3 M KOH from which usually practically available C_S of a single electrode is calculated. The rate dependent discharge profile for pristine TiO₂ and Zr:TiO₂ are given in ESI† (S7). The discharge curve is observed to be a combination of three

processes, viz. (i) a fast initial potential drop followed by (ii) a slow potential decay, and (iii) a faster voltage drop corresponding to EDLC. The first two sections (Fig. 5b) are assigned to the reduction Ti^{4+} to Ti^{3+} as observed from the CVs. The clear non-linear shape of the discharge curves and the deviation from rectangular shape of the CV (Fig. 3d) reveal that the major contribution of C_S of Nb:TiO₂ electrode material originates from faradic reactions.

The C_S was calculated from the charge – discharge curves using the relation

$$C_S = \frac{It}{m\Delta V} \quad (4)$$

where I , t , m and ΔV are applied current, time, active mass, and potential range of the charging and discharging events, respectively. Insets of Fig. 5b shows the C_S calculated from galvanostatic discharge curves as a function of specific current density. The C_S decreased with increasing current density similar to that observed in the CV measurements. The contribution of C_S from the substrate was also studied in 3 M KOH from the discharge curves without using the nanowires (See ESI†, S5). The discharge time was 5 s for Ni foam alone; thereby demonstrating that capacitive contribution from the substrate could be neglected.

Effects of the high crystallinity and clear insertion/exertion pathways of the electrospun Nb:TiO₂ nanowires are more evident in the cycling stability of the electrodes fabricated in this study. Fig. 5c shows the stability of electrochemical cycling of the Nb:TiO₂ nanowires. The electrodes showed good cycling behaviour with ~100% retention in C_S at the end of 5000 cycles. The electrode was also physically stable; no peeling-off of the electrode material from current collector was observed even after 5000 cycles. The Coulombic efficiency calculated from ratio of the discharging to the charging times during the charge–discharge cycling was ~100% and remind practically same during cycling.

3.4 Electrochemical impedance spectroscopy

The EIS measurements were carried out to determine the electrode kinetics. Figure 5d shows the Nyquist plot of nanowire electrodes determined by electrochemical impedance spectroscopy (EIS) in the frequency range 100 kHz – 0.01 Hz at open circuit potential in 3 M KOH. The EIS spectra of a SC electrode usually divided into three segments following three processes; (i) the bulk resistance of the device (R_S), synonymously called equivalent series resistance (ESR) at high frequency ($> 1\text{kHz}$); (ii) capacitive effects at intermediate frequencies ($1 - 0.1\text{ kHz}$); and (iii) Warburg diffusion resulting from the frequency dependence of ion diffusion/ transport in the electrolyte at the low frequencies ($<0.1\text{ Hz}$). The R_S is a combination of (i) electrolyte resistance, (ii) intrinsic resistance of the electro active material, and (iii) the contact resistance between the active material and the current collector that determines the high frequency off-set of the EIS spectrum. The value of R_S determined from the high frequency off-set of the EIS spectra is $\sim 2.8\ \Omega$, $4.5\ \Omega$ and $6.7\ \Omega$ for Nb:TiO₂, Zr:TiO₂ and pristine TiO₂ respectively. The lower R_S value of Nb:TiO₂ could be attributed to the high electrical conductivity of the present Nb:TiO₂ nanowires in addition to the one-dimensional morphology and ultrafine wire diameter.

Similarly the electrochemical performance of AC electrode was also evaluated in a three electrode configuration (See ESI†, S8). The CV curves of the AC electrode at different scan rates in 3 M KOH aqueous electrolyte shows nearly rectangular shapes, suggesting that the AC electrode is an excellent choice to fabricate electric double layer capacitance (EDLC). The C_S of the material is estimated at $82\ \text{Fg}^{-1}$. Furthermore, the galvanostatic charge discharge curves of the AC measured at different current densities are symmetric and linear, which clearly shows the EDLC of the AC electrode. The C_S values of the AC electrodes are estimated using the equation 4 to be 82, 80, and 74 at $1\ \text{Ag}^{-1}$, $2\ \text{Ag}^{-1}$ and $5\ \text{Ag}^{-1}$ respectively.

3.5 Practical Asymmetric Supercapacitor

To evaluate the capacitive performance of the Nb:TiO₂ electrode in a full device configuration, an asymmetric supercapacitor (ASC) device was fabricated by using Nb:TiO₂ as the anode activated carbon (AC) as cathode. It is imperative to understand the properties of the pseudocapacitive and carbon electrodes separately for fabrication ASCs for optimum performance. This is because an ASC is equivalent to two capacitors in series whose reciprocal of the effective capacitance is equal to the sum of the reciprocals of the individual capacitances ($\frac{1}{C_{eff}} = \frac{1}{C_{anode}} + \frac{1}{C_{cathode}}$). This relation follows that the effective capacitance will be lower than the lowest individual capacitance. Therefore, both electrodes of ASCs should have similar capacitance for maximum effective capacitance²⁶. The similarity in capacitance follows a charge balance (as charge $q = CV$) $q_+ = q_-$, where q_+ is the charge stored at the anode and q_- is that at the cathode. The charge on each electrode is given by $q = C_s \times \Delta V \times m$ ²⁷, where ΔV is the potential window, from which the mass on the respective electrode for optimum performance follows^{28,26}

$$\frac{m_-}{m_+} = \frac{C_{S+}(PC) \times \Delta V_+}{C_{S-}(EDLC) \times \Delta V_-} \quad (5)$$

On the basis of the C_s values and potential windows of the Nb:TiO₂ and AC electrodes determined separately as explained above, the optimised mass ratio for fabrication of ASC was calculated to be ~1.5. A total of four ASCs were fabricated with cathode mass-loading up to 3.7 mg and anode mass-loading up to 2.5 mg to confirm the consistence of the results. A couple of symmetric EDLC using the AC electrodes (mass loading of ~4.2 mg on each electrodes) was fabricated as a control device. The devices had a geometric surface area of ~1cm².

Fig. 6(a&b) shows the CV curves of the AC//AC symmetric EDLC and the Nb:TiO₂//AC ASCs devices as a function of scan rates, respectively. The ASC cell voltage can be expressed as the sum of the potential window of Nb:TiO₂ anode and AC cathode, which shows that potential window is between 0.5 V and -1.0 V vs. Ag/AgCl (see ESI†, S7). Therefore, the Nb:TiO₂//AC device could achieve a maximum voltage of 1.5 V. Nearly rectangular shape and scan independent shape of CV curves (Fig. 6a) of the symmetric capacitors shows that the capacitance originates from EDLC. In addition, no scan rate dependence on C_S was observed (Inset of Fig. 6a). On the other hand, the CV curves of the ASC (Fig. 6b) exhibited regions with and without redox peaks characterizing faradic pseudocapacitance and EDLC, respectively. The inset of Fig. 6b shows the C_S calculated from the CV curves. A scan rate dependence on C_S was observed thereby revealing that the charge storage capabilities of the present ASC dominated by the Nb:TiO₂ electrode material.

The electrochemical performance was also measured by galvanostatic charge-discharge at current densities from 1 to 15 Ag⁻¹. Fig. 6(c&d) shows the first three charge-discharge cycles at a current density of ~1 Ag⁻¹ of the EDLC and ASC devices. Maximum achievable potential window in the EDLC was ~1.2 V (Data for V~ 1.5 V is in ESI†, S10) whereas that in the ASC was ~1.5 V. The additional voltage (0.3 V) achieved in the ASC is expected to originate from the pseudocapacitive reaction in the Nb:TiO₂ electrode. Figure 6(e&f) are the discharge curves at different current densities to evaluate the rate capability of the devices and quantify the C_S . The insets of the respective figures show the variation of C_S as a function of current density determined following the Eq (4). The C_S decreases with increase in current density because the movements of electrolyte ions are limited to the surface of the electrode at high current densities whereas bulk diffusion occurs at lower values. The maximum C_S of symmetric EDLC was 17 Fg⁻¹ at a discharge current density of 1

Ag^{-1} whereas that of ASC was nearly three times higher (52 Fg^{-1}). Therefore, due to the higher V and C_S , ASC is expected to have more than three-fold charge storage capability than the symmetric EDLC.

The operational stability of the device was evaluated by galvanostatic CDC at (i) single current rating ($\sim 5 \text{ Ag}^{-1}$) and (ii) progressively varying current densities ($1 - 5 \text{ Ag}^{-1}$). The ASC exhibited capacitive retention of $\sim 100\%$ and Coulombic efficiency of $\sim 100\%$ at the end of the 3000 cycles (Fig. 7a) at 1 Ag^{-1} . Fig. 7b shows the rate capability of the device at current densities 1, 2, and 5 Ag^{-1} . The device retained nearly constant C_S upon cycling at each current density. After continuous cycling for 1500 cycles at different current densities and when the current density is brought back to 1 Ag^{-1} for the last 500 cycles, the C_S remained without any loss (Fig. 7b). The C_S retention at a high current rating is superior to those reported for asymmetric supercapacitors using AC as an anode (Table 3).

Fig. 7c shows the Nyquist plot of the EDLC and ASC devices determined by EIS in the frequency range $10 \text{ kHz} - 0.01 \text{ Hz}$ at open circuit potential in the 3 M KOH electrolyte²⁹. The value of R_S determined from the high frequency off-set of the EIS spectra for the ASC is $\sim 0.45 \Omega$ which is desirable for a high power density; whereas R_S of EDLC is 0.88Ω . The E_S and P_S of the devices were calculated using the relations

$$\left. \begin{aligned} E_S &= \frac{1}{2} C_S V^2; \\ P_S &= \frac{E_S}{\Delta t} \end{aligned} \right\} \quad (6)$$

Fig. 7d shows the Ragone plot which relates the P_S with the E_S . The ASC delivered E_S of 16.3, 11.4 and 5.6 Whkg^{-1} at P_S of 770, 1310, and 1900 Wkg^{-1} , respectively. On the other hand, performance of the control EDLC is much inferior. The EDLC delivered E_S of 4.9, 4.5 and 4.2 Whkg^{-1} at P_S 180, 317 and 690 Wkg^{-1} , respectively.

Finally, we compare the performance of the present ASCs with other devices employing various TMOs as anode and the AC as the cathode in aqueous electrolyte (Table 3). Although there are many ASCs reported with TMO+ carbon nanotubes(CNT)/graphene as anode and CNT/graphene as cathodes, details of which are available in a recent review article³⁰, they are omitted from the present comparison for the sake of simplicity. Indeed, there are a number of devices such as Ni(OH)₂//AC³¹ and Ni_{0.61}Co_{0.39}O//AC ASCs³² reported in literature with higher E_S ; but all of them suffers from cycling stability than the performance achieved in this work. The higher E_S with high cycling stability could be attributed to the high electrical conductivity of the highly crystalline nanowires electrode. The Nb:TiO₂ based device shows 100% retention at the end of 5000 cycles which is suitable for a commercial device. Moreover, the current device could achieve a higher potential window of ~1.5 V in environmentally benign and low cost aqueous KOH electrolyte, which is comparable to those of commercial alkaline batteries. The potential window of the present Nb:TiO₂-based device could be increased further using proper another cathode material or using composite anode in the same electrolyte.

Conclusions

In conclusion, we have shown that Nb:TiO₂ nanowires have an order of magnitude higher specific capacitance than pristine and Zr:TiO₂, which could be assigned to its improved electrical conductivity. Cyclic voltammetric measurements show that the superior electrical conductivity of Nb:TiO₂ help the electrode to achieve two orders of magnitude higher ion diffusivity ($1.08 \times 10^{-13} \text{ cm}^2 \text{ s}^{-1}$) than that offered by the other electrodes in this study ($9.16 \times 10^{-15} \text{ cm}^2 \text{ s}^{-1}$) and has 100% Coulombic efficiency. The improved electrical conductivity, ion diffusivity, and Coulombic efficiency enable the Nb:TiO₂ electrode to show constant capacitance for over 5000 cycles. A practical supercapacitor fabricated in

asymmetric configuration using the Nb:TiO₂ as anode and activated carbon as cathode gave energy densities of 16.3, 11.4 and 5.6 Whkg⁻¹ at power densities of 770, 1310, and 1900 Wkg⁻¹, respectively, which are much superior to a control device fabricated using activated carbon as its both electrodes. High abundance of TiO₂ in the earth's crust and promising results achieved herewith offer unique opportunities to develop practical supercapacitors at lower costs.

Acknowledgements

This work is supported by the Research and Innovation Department (RDU 150325) of Universiti Malaysia Pahang.

†Electronic Supplementary Information (ESI) Available: S1 – details of calculation of theoretical capacitance of TiO₂; S2 – X-ray fluorescence spectra of the doped materials; S3 – results of electrochemical analysis of 5 at.% Nb:TiO₂; S4 – details of calculation of the ion diffusion in the electrodes; S5 – background capacitance from the nickel foam substrate; S6 – first three discharge curves showing the internal resistance of the electrodes and details of calculation; S7 – discharge curves of pristine TiO₂ and Zr:TiO₂; S8 – electrochemical characterization of activated carbon electrodes in the 3-electrode configuration in 3 M KOH aqueous electrolyte; S9 – cyclic voltammograms showing maximum achievable capacitance in the practical asymmetric supercapacitor; S10 – cyclic voltammograms of AC//AC symmetric EDLC at various scan rates in the potential window 1.5 V in 3 M KOH electrolyte. See doi: (to be inserted by the RSC staff)

References:

1. D. Yu, Q. Qian, L. Wei, W. Jiang, K. Goh, J. Wei, J. Zhang, and Y. Chen, *Chem. Soc. Rev.*, 2015, **44**, 647–662.
2. D. R. Rolison and L. F. Nazar, *MRS Bull.*, 2011, **36**, 486–493.
3. D. A. J. Rand, *J. Solid State Electrochem.*, 2011, **15**, 1579–1622.
4. N.-S. Choi, Z. Chen, S. a Freunberger, X. Ji, Y.-K. Sun, K. Amine, G. Yushin, L. F. Nazar, J. Cho, and P. G. Bruce, *Angew. Chem. Int. Ed. Engl.*, 2012, **51**, 9994–10024.
5. S. Liu, S. Sun, and X.-Z. You, *Nanoscale*, 2014, **6**, 2037–45.
6. P. J. Hall, M. Mirzaeian, S. I. Fletcher, F. B. Sillars, A. J. R. Rennie, G. O. Shitta-bey, G. Wilson, and R. Carter, *Energy Environ. Sci.*, 2010, **3**, 1238–1251.
7. H. Li, J. Wang, Q. Chu, Z. Wang, F. Zhang, and S. Wang, *J. Power Sources*, 2009, **190**, 578–586.
8. J. Tian, Z. Zhao, A. Kumar, R. I. Boughton, and H. Liu, *Chem. Soc. Rev.*, 2014, **43**, 6920 – 6937.
9. R. Jose, V. Thavasi, and S. Ramakrishna, *J. Am. Ceram. Soc.*, 2009, **92**, 289–301.
10. M. V Reddy, G. V. S. Rao, and B. V. R. Chowdari, *Chem. Rev.*, 2013, **113**, 5364 – 5457.
11. Y. Furubayashi, T. Hitosugi, Y. Yamamoto, K. Inaba, G. Kinoda, Y. Hirose, T. Shimada, and T. Hasegawa, *Appl. Phys. Lett.*, 2005, **86**, 1–3.
12. F. Fabregat-santiago, E. M. Barea, J. Bisquert, G. K. Mor, K. Shankar, and C. a Grimes, *J. Am. Chem. Soc.*, 2008, **130**, 11312–11316.
13. P. S. Archana, A. Gupta, M. M. Yusoff, and R. Jose, *Phys. Chem. Chem. Phys.*, 2014, **16**, 7448–54.
14. P. S. Archana, A. Gupta, M. M. Yusoff, and R. Jose, *Appl. Phys. Lett.*, 2014, **105**, 153901–5.
15. P. S. Archana, E. Naveen Kumar, C. Vijila, S. Ramakrishna, M. M. Yusoff, and R. Jose, *Dalt. Trans.*, 2012, **42**, 1024–1032.
16. P. S. Archana, R. Jose, T. M. Jin, C. Vijila, M. M. Yusoff, and S. Ramakrishna, *J. Am. Ceram. Soc.*, 2010, **93**, 4096–4102.

17. T. Hitosugi, H. Kamisaka, K. Yamashita, H. Nogawa, Y. Furubayashi, S. Nakao, N. Yamada, A. Chikamatsu, H. Kumigashira, M. Oshima, Y. Hirose, T. Shimada, and T. Hasegawa, *Appl. Phys. Express*, 2008, **1**, 1112031–1112033.
18. S. Ramakrishna, R. Jose, P. S. Archana, a. S. Nair, R. Balamurugan, J. Venugopal, and W. E. Teo, *J. Mater. Sci.*, 2010, **45**, 6283–6312.
19. P. S. Archana, R. Jose, C. Vijila, and S. Ramakrishna, *J. Phys. Chem. C*, 2009, **113**, 21538–21542.
20. B. Vidhyadharan, N. Khayyriah, M. Zain, I. I. Misnon, R. A. Aziz, J. Ismail, M. M. Yusoff, and R. Jose, *J. Alloys Compd.*, 2014, **610**, 143–150.
21. P. Vishnu Kamath and M. F. Ahmed, *J. Appl. Electrochem.*, 1993, **23**, 225–230.
22. L. Bing, Y. Huatang, Z. Yunshi, Z. Zuoxiang, and S. Deying, *J. Power Sources*, 1999, **79**, 277–280.
23. E. Shangguan, Z. Chang, H. Tang, X.-Z. Yuan, and H. Wang, *J. Power Sources*, 2011, **196**, 7797–7805.
24. X. Cao, J. Wei, Y. Luo, Z. Zhou, and Y. Zhang, *Int. J. Hydrogen Energy*, 2000, **25**, 643–647.
25. B. Shruthi, V. Bheema Raju, and B. J. Madhu, *Spectrochim. Acta. A. Mol. Biomol. Spectrosc.*, 2015, **135**, 683–9.
26. P. Tang, Y. Zhao, C. Xu, and K. Ni, *J. Solid State Electrochem.*, 2013, **17**, 1701–1710.
27. D. Zhang, K. Ryu, X. Liu, E. Polikarpov, J. Ly, M. E. Tompson, and C. Zhou, *Nano Lett.*, 2006, **6**, 1880–6.
28. P. Chen, G. Shen, Y. Shi, H. Chen, and C. Zhou, *ACS Nano*, 2010, **4**, 4403–4411.
29. Y. Q. Zhang, L. Li, S. J. Shi, Q. Q. Xiong, X. Y. Zhao, X. L. Wang, C. D. Gu, and J. P. Tu, *J. Power Sources*, 2014, **256**, 200–205.
30. F. Wang, S. Xiao, Y. Hou, C. Hu, L. Liu, and Y. Wu, *RSC Adv.*, 2013, **3**, 13059–13084.
31. J. Huang, P. Xu, D. Cao, X. Zhou, S. Yang, Y. Li, and G. Wang, *J. Power Sources*, 2014, **246**, 371–376.
32. Y. Wang, X. Zhang, C. Guo, Y. Zhao, C. Xu, and H. Li, *J. Mater. Chem. A*, 2013, **1**, 13290–13300.
33. G. Wang, Z. Y. Liu, J. N. Wu, and Q. Lu, *Mater. Lett.*, 2012, **71**, 120–122.

34. M. Salari, S. H. Aboutalebi, A. T. Chidembo, K. Konstantinov, and H. K. Liu, *J. Alloys Compd.*, 2014, **586**, 197–201.
35. X. Lu, G. Wang, T. Zhai, M. Yu, J. Gan, Y. Tong, and Y. Li, *Nano Energy*, 2012, **12**, 1690–1696.
36. M. Salari, S. H. Aboutalebi, A. T. Chidembo, I. P. Nevirkovets, K. Konstantinov, and H. K. Liu, *Phys. Chem. Chem. Phys.*, 2012, **14**, 4770–4779.
37. A. Ramadoss and S. J. Kim, *Carbon N. Y.*, 2013, **63**, 434–445.
38. S. Dong, X. Chen, L. Gu, X. Zhou, H. Xu, H. Wang, Z. Liu, P. Han, J. Yao, L. Wang, G. Cui, and L. Chen, *ACS Appl. Mater. Interfaces*, 2011, **3**, 93–98.
39. G. D. Moon, J. B. Joo, M. Dahl, H. Jung, and Y. Yin, *Adv. Funct. Mater.*, 2014, **24**, 848–856.
40. C. C. Hu, C. W. Wang, T. H. Wu, and K. H. Chang, *Electrochim. Acta*, 2012, **85**, 90–98.
41. H. Li, Z. Chen, C. K. Tsang, Z. Li, X. Ran, C. Lee, B. Nie, L. Zheng, T. Hung, J. Lu, B. Pan, and Y. Y. Li, *J. Mater. Chem. A*, 2014, **2**, 229–236.
42. F. Fabregat-Santiago, H. Randriamahazaka, A. Zaban, J. Garcia-Cañadas, G. Garcia-Belmonte, and J. Bisquert, *Phys. Chem. Chem. Phys.*, 2006, **8**, 1827–1833.
43. H. Liang, F. Chen, R. Li, L. Wang, and Z. Deng, *Electrochim. Acta*, 2004, **49**, 3463–3467.
44. B. Chen, J. Hou, and K. Lu, *Langmuir*, 2013, **29**, 5911–5919.
45. W. W. Liu, X. B. Yan, and Q. J. Xue, *J. Mater. Chem. C*, 2013, **1**, 1413–1422.
46. D. Luo, Y. Li, J. Liu, H. Feng, D. Qian, S. Peng, J. Jiang, and Y. Liu, *J. Alloys Compd.*, 2013, **581**, 303–307.
47. P.-C. Chen, S.-J. Hsieh, J. Zou, and C.-C. Chen, *Mater. Lett.*, 2014, **133**, 175–178.
48. A. Ramadoss and S. J. Kim, *Int. J. Hydrogen Energy*, 2014, **39**, 12201–12212.
49. C. Huang, N. P. Young, and P. Grant, *J. Mater. Chem. A*, 2014, **2**, 11022–11028.
50. H. Zhou, Y. Zhong, Z. He, L. Zhang, J. Wang, J. Zhang, and C. N. Cao, *J. Alloys Compd.*, 2014, **597**, 1–7.
51. B. Zhang, R. Shi, Y. Zhang, and C. Pan, *Prog. Nat. Sci. Mater. Int.*, 2013, **23**, 164–169.

52. Y. Xiao, S. Liu, F. Li, A. Zhang, J. Zhao, S. Fang, and D. Jia, *Adv. Funct. Mater.*, 2012, **22**, 4052–4059.
53. Y. Gong, F. Gong, C. Wang, H. Zheng, and F. Li, *RSC Adv.*, 2015, **5**, 27266–27272.
54. Y. Xiao, A. Zhang, S. Liu, J. Zhao, S. Fang, D. Jia, and F. Li, *J. Power Sources*, 2012, **219**, 140–146.
55. C. Zhang, L. Xie, W. Song, J. Wang, G. Sun, and K. Li, *J. Electroanal. Chem.*, 2013, **706**, 1–6.
56. X. Du, C. Wang, M. Chen, Y. Jiao, and J. Wang, *J. Phys. Chem. C*, 2009, **113**, 2643–2646.
57. C.-S. Dai, P.-Y. Chien, J.-Y. Lin, S.-W. Chou, W.-K. Wu, P.-H. Li, K.-Y. Wu, and T.-W. Lin, *ACS Appl. Mater. Interfaces*, 2013, **5**, 12168–74.
58. X. Wang, C. Yan, A. Sumboja, and P. S. Lee, *Nano Energy*, 2014, **3**, 119–126.
59. C.-H. Lien, C.-C. Hu, C.-T. Hsu, and D. S.-H. Wong, *Electrochem. commun.*, 2013, **34**, 323–326.
60. C. Tang, X. Yin, and H. Gong, *ACS Appl. Mater. Interfaces*, 2013, **5**, 10574–82.
61. S. T. Senthilkumar, R. K. Selvan, M. Ulaganathan, and J. S. Melo, *Electrochim. Acta*, 2014, **115**, 518–524.
62. M.-C. Liu, L. Kang, L.-B. Kong, C. Lu, X.-J. Ma, X.-M. Li, and Y.-C. Luo, *RSC Adv.*, 2013, **3**, 6472–6478.
63. J.-G. Wang, Y. Yang, Z.-H. Huang, and F. Kang, *Carbon N. Y.*, 2013, **61**, 190–199.
64. Y. Tang, Y. Liu, S. Yu, Y. Zhao, S. Mu, and F. Gao, *Electrochim. Acta*, 2014, **123**, 158–166.
65. X. Zhang, X. Sun, H. Zhang, D. Zhang, and Y. Ma, *Mater. Chem. Phys.*, 2012, **137**, 290–296.
66. P. Sivaraman, A. R. Bhattacharaya, S. P. Mishra, A. P. Thakur, K. Shashidhara, and A. B. Samui, *Electrochim. Acta*, 2013, **94**, 182–191.
67. Y.-G. Wang, Z.-D. Wang, and Y.-Y. Xia, *Electrochim. Acta*, 2005, **50**, 5641–5646.
68. L.-J. Xie, J.-F. Wu, C.-M. Chen, C.-M. Zhang, L. Wan, J.-L. Wang, Q.-Q. Kong, C.-X. Lv, K.-X. Li, and G.-H. Sun, *J. Power Sources*, 2013, **242**, 148–156.
69. Y. Xue, Y. Chen, M.-L. Zhang, and Y.-D. Yan, *Mater. Lett.*, 2008, **62**, 3884–3886.

70. Y. Tang, Y. Liu, S. Yu, S. Mu, S. Xiao, Y. Zhao, and F. Gao, *J. Power Sources*, 2014, **256**, 160–169.
71. B. Vidyadharan, R. A. Aziz, I. I. Misnon, G. M. Anil Kumar, J. Ismail, M. M. Yusoff, and R. Jose, *J. Power Sources*, 2014, **270**, 526–535.
72. X. Wang, J. Liu, Y. Wang, C. Zhao, and W. Zheng, *Mater. Res. Bull.*, 2014, **52**, 89–95.
73. F. X. Wang, S. Y. Xiao, Y. S. Zhu, Z. Chang, C. L. Hu, Y. P. Wu, and R. Holze, *J. Power Sources*, 2014, **246**, 19–23.
74. J.-W. Lang, L.-B. Kong, M. Liu, Y.-C. Luo, and L. Kang, *J. Solid State Electrochem.*, 2009, **14**, 1533–1539.
75. C.-T. Hsu and C.-C. Hu, *J. Power Sources*, 2013, **242**, 662–671.
76. B. Senthilkumar, D. Meyrick, Y.-S. Lee, and R. K. Selvan, *RSC Adv.*, 2013, **3**, 16542–16548.
77. X. Zhang, Y. Zhao, and C. Xu, *Nanoscale*, 2014, **6**, 3638–46.
78. Y. Cao, Y. Xiao, Y. Gong, C. Wang, and F. Li, *Electrochim. Acta*, 2014, **127**, 200–207.

Table 1: Lattice parameters of pristine and doped TiO₂

Phase	Lattice parameters (Å)	
	a	c
TiO ₂	3.785(3)	9.501(2)
2at.% Nb:TiO ₂	3.783(7)	9.501(2)
2at.% Zr:TiO ₂	3.782(5)	9.499(7)

Table 2: Summary of research describing the electrochemical properties of TiO₂ electrode

Morphology	Method of synthesis	C _S (Fg ⁻¹)	C _S Retention(%)/Cycle number	Scan rate/ Current density	Electrolyte	Ref
TiO ₂ -B nanotubes	Solvothermal reaction	17.7	NR	NR	NR	33
TiO ₂ nanotubes	Anodisation	911 μFcm ⁻²	NR	NR	NR	34
TiO ₂ Powder	Sol-gel	181 μFcm ⁻²				34
Hydrogenated TiO ₂ Nanotube	Anodic oxidation	3.24 mFcm ⁻² 0.03 mFcm ⁻²	NR	100 mVs ⁻¹	NR	35
TiO ₂ nanotube array	Anodic oxidation	19.2	NR	1 mVs ⁻¹	NR	36
TiO ₂ particles on graphene sheet	NR	165	90/(5000)	5 mVs ⁻¹	1 M Na ₂ SO ₄	37
TiN spheres	Template free	133	NR	2 mVs ⁻¹	NR	38
TiO ₂ hollow nanoshells	NR	7.1 mFcm ⁻²	NR	NR	NR	39
RuO ₂ -xH ₂ O-TiO ₂ nanoflowers	NR	425	NR	25 mVs ⁻¹	NR	40
TiO ₂	NR	2.6	NR	50 mAc ⁻²	NR	41
TiO ₂ nanotubes	Anodization	6 mFcm ⁻²				12
Nanoporous TiO ₂	NR	NR	NR	NR	0.1 M KPF ₆	42
Activated carbon modified TiO ₂	NR	63.1	NR	NR	NR	43
TiO ₂ nanotube	anodization	3.4 mFcm ⁻²	NR	NR	1 M KCl	44
GNS/TiO ₂ film	NR	0.86 mFcm ⁻²	98/(1500)	10 mVs ⁻¹	0.5 M Na ₂ SO ₄	45
RGO-Cu ₂ OTiO ₂	NR	80	98/(1000)	0.2 Ag ⁻¹	6 M KOH	46
Ti/TiO ₂	NR	35.5	NR	NR	NR	47

Self assembled	NR	1.6 mFcm ⁻²	97/(1000)	1 mVs ⁻¹	1 M NaOH	34
TiO ₂ @MnO ₂	NR	22.2 mFcm ⁻²	85/(4000)	5 mVs ⁻¹	1 M Na ₂ SO ₄	48
Nanowall arrays						
TiO ₂ nanoparticles/ carbon nanotube	NR	145	NR	2 mVs ⁻¹	NR	49
3D nanoporous H-TiO ₂	NR	1.1 mFcm ⁻²	NR	100 mVs ⁻¹	NR	50
CNT/TiO ₂ nanocomposite	NR	6.9 Fg ⁻¹	NR	NR	NR	51
3 D Hierarchical Co ₃ O ₄	Solvothermal	781	98/1000	0.5 Ag ⁻¹	KOH	52
Co ₃ O ₄ nanospheres	NR	1100	85/5000	1 Ag ⁻¹	6 M KOH	53
Cobalt Cobaltit nanowalls	calcination	997	93/1000	0.5 Ag ⁻¹	KOH	54

NR – Not reported.

Table 3: Comparison of energy storage parameters of ASC devices employing other TMOs reported in literature with that of the present Nb:TiO₂//AC ASCs. GR = graphene; NR = not reported; PMT = poly(3-methyl thiophene); PPy = polypyrrole.

ASC Configuration	Electrolyte	C_S (Fg ⁻¹)	Max V	E_S (Wh.kg ⁻¹) @ P_S (kW.kg ⁻¹)	C_S retention (%) /cycle number	Ref.
Ni(OH) ₂ //AC	6M KOH	105	1.6	36.2@0.1	92/1000	31
Ni _{0.61} Co _{0.39} O//AC	2M KOH	130.2	1.5	36.5@0.1	62.16/1000	32
Co ₃ O ₄ //AC	6M KOH	81	1.5	24.9@0.2	90/5000	55
Fe ₃ O ₄ //AC	6M KOH	37	1.2	NR	82/500	56
Ni ₃ S ₂ //AC	2M KOH	55.8	1.6	19.8@0.8	90/5000	57
Ni _x Co _{3-x} O ₄ //AC	2M KOH	105	1.6	37.4@0.2	82.8/3000	58
Ni-Co-Cu oxy hydroxide//AC	1M NaOH	58	1.8	NR	94.5/4000	59
Co ₃ O ₄ @NiOH //AC	6M KOH	110.6	1.7	41.9@0.4	81/1000	60
α-Bi ₂ O ₃ //AC	Li ₂ SO ₄	29	1.6	10.2@0.8	72/1000	61
NiMoO ₄ .xH ₂ O//AC	2M KOH	96.7	1.6	34.4@0.1	80.6/1000	62
MnO ₂ -C//AC	0.5M NaSO ₄	56.8	2	30.6@0.2	6/5000	63
Ni(OH) ₂ -TH-NH ₃	NR	87.8	1.6	32.7@0.071	NR	64
MnO ₂ -AC//AC	1M Na ₂ SO ₄	50.6	2	9.7@0.1	86/1000	65
PMT/MWNT//AC	TEABF ₄	38.5	2.5	33.4@NR	85/1200	66
RuO ₂ /TiO ₂ //AC	1M KOH	46	1.4	12.5@0.1	90/1000	67
Co ₃ O ₄ -rGO//AC	6M KOH	114.1	1.5	35.7@0.2	95/1000	68
λ-MnO ₂ //AC	1M LiSO ₄	53	2.2	36@0.3	NR	69
Co(OH) ₂ //AC	6M KOH	38.9	1.6	13.6@0.1	NR	70
Co ₃ O ₄ //AC	6M KOH	175	1.4	47.6@1.4	97/2000	71
Ni(OH) ₂ /GN/NF//AC	6M KOH	80	1.4	11.1@NR	NR	72
LiMn ₂ O ₄ //AC	1M LiSO ₄	NR	1.8	29.8@0.09	91/1000	73
α-Ni(OH) ₂ //AC	2M KOH	127	1.2	42@0.1	82/1000	74

NiCo ₂ O ₄ //AC	1M NaOH	NR	1.7	17.7@NR	100/2000	75
NiMoO ₄ -	2M NaOH	80	1.4	28@0.1	92/1000	76
CoMoO ₄ //AC						
Co ₃ O ₄ //AC	6M KOH	107.3	1.5	34@0.22	98/1500	77
MnOOH@RGO//AC	6 M KOH	115.6	1.6	41.1@0.4	98/5000	78
Nb:TiO ₂ //AC	3M KOH	52	1.5	16.3@0.77	100/5000	This work

Figure captions

Figure 1: The XRD patterns of TiO₂, Zr:TiO₂ and Nb:TiO₂ nanowires. The inset shows the peak corresponding to the (107) plane showing a minor shift in its position.

Figure 2: (a, b & c) SEM images and (a₁, b₁ & c₁) TEM images of TiO₂, Nb:TiO₂ and Zr:TiO₂ respectively

Figure 3:(a) shows the CV of the electrodes at a scan rate 2 mVs⁻¹ (b, c & d) CV curves of pristine TiO₂, Zr:TiO₂ and Nb:TiO₂ electrodes in 3 M KOH aqueous electrolyte at scan rate between 1 to 60 mVs⁻¹ with respect to Ag/AgCl reference electrode.

Figure 4: (a) Variation in C_s with scan rates;(b&d) anodic peak current verses square root of scan rate in pristine TiO₂ and Nb:TiO₂ indicating bulk diffusion of ions during the Faradic process; (c) anodic peak current verses scan rate in Zr:TiO₂

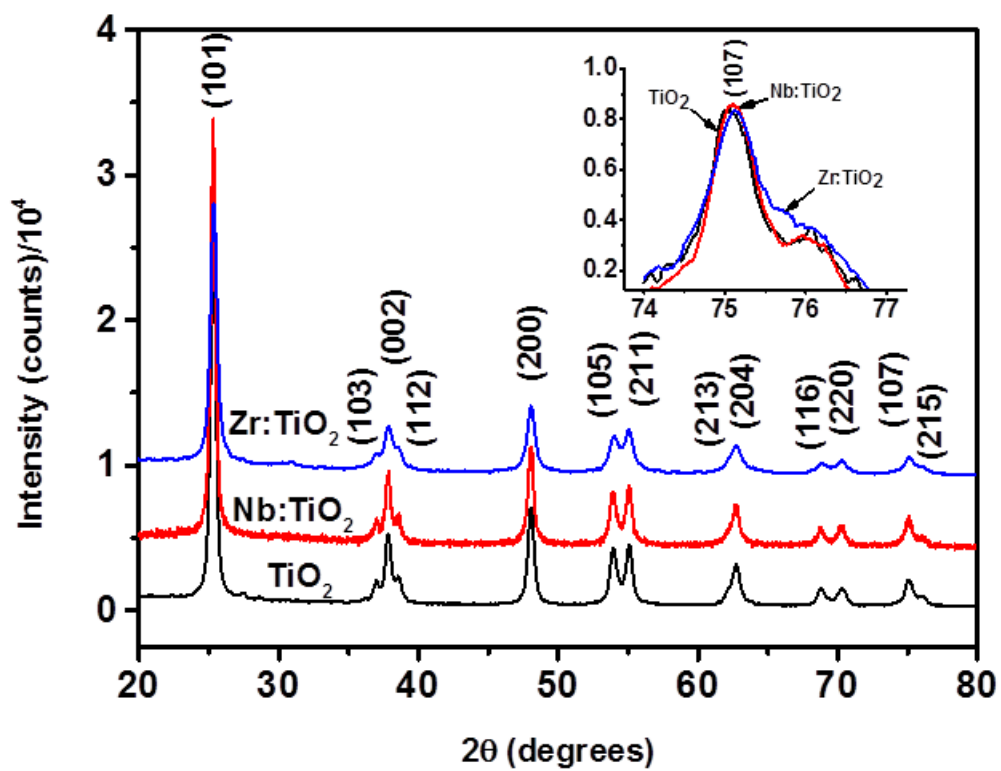
Figure 5: (a) discharge curves of all 3 electrodes in 3 M KOH aqueous electrolyte at a galvanostatic current density of 1 Ag⁻¹ (b) discharge curves of Nb:TiO₂ electrode at different current densities in 3 M KOH aqueous electrolyte (c)Dependence of discharge C_s and Coulombic efficiency as a function of charge discharge cycle numbers (d) Nyquist plot for all 3 electrodes at open circuit potential; inset show the expanded high frequency region.

Figure 6: (a) The CV data of the AC//AC symmetric capacitor in 3 M KOH aqueous electrolyte at scan rates between 5 and 60 mVs⁻¹;inset shows variation C_s with scan rate (b) The CV data of the Nb:TiO₂//AC asymmetric supercapacitor in 3 M KOH aqueous electrolyte at scan rates between 2 and 60 mVs⁻¹;inset shows variation in C_s with scan rate (c) The first three charge – discharge curves of the AC//AC symmetric supercapacitor in 3 M KOH aqueous electrolyte at a galvanostatic current density of 1 Ag⁻¹ (d) The first three charge – discharge curves of the Nb:TiO₂//AC asymmetric capacitor in 3 M KOH aqueous solution at a galvanostatic current density of 1 Ag⁻¹ (e) The discharge curves of the AC//AC symmetric capacitor at different current densities in 3 M KOH aqueous electrolyte; inset variation of specific capacitance of the device calculated from discharge curves (f) The discharge curves of the Nb:TiO₂//AC asymmetric capacitor at

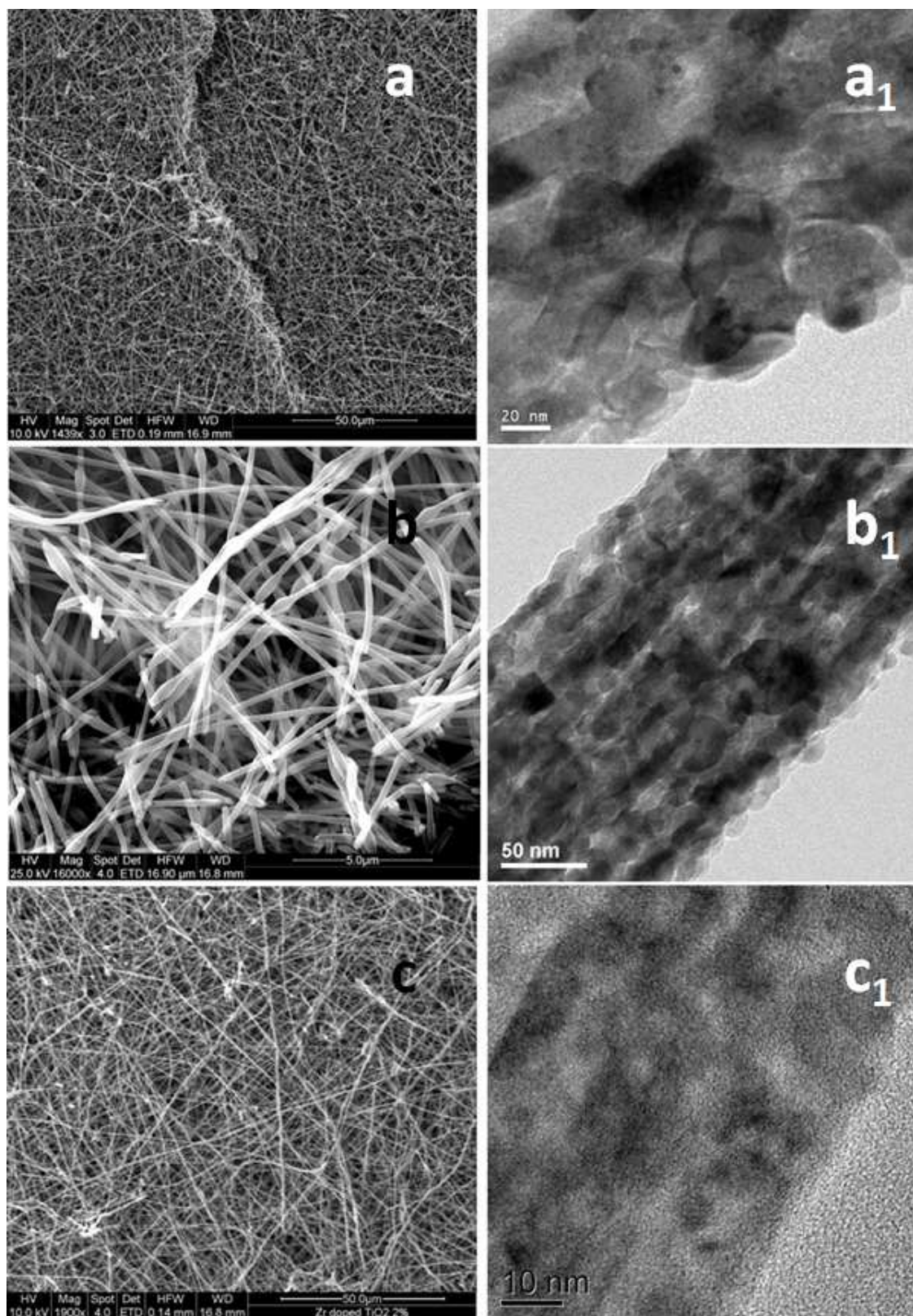
different current densities in 3 M KOH aqueous solution; inset shows the variation of C_S of the device calculated from discharge curves.

Figure 7: (a) Dependence of the discharge C_S and the columbic efficiency as a function of charge –discharge cycle numbers. The charge – discharge tests were performed at 5 Ag^{-1} in 3 M KOH aqueous electrolyte (b) dependence of the discharge C_S as a function of charge –discharge cycle numbers at progressively varying current densities.(c) Nyquist plot for both AC//AC and Nb:TiO₂//AC devices at open circuit potential. Insets show the expanded high frequency regions (d) Comparative Ragone plots of the symmetric and asymmetric supercapacitors.

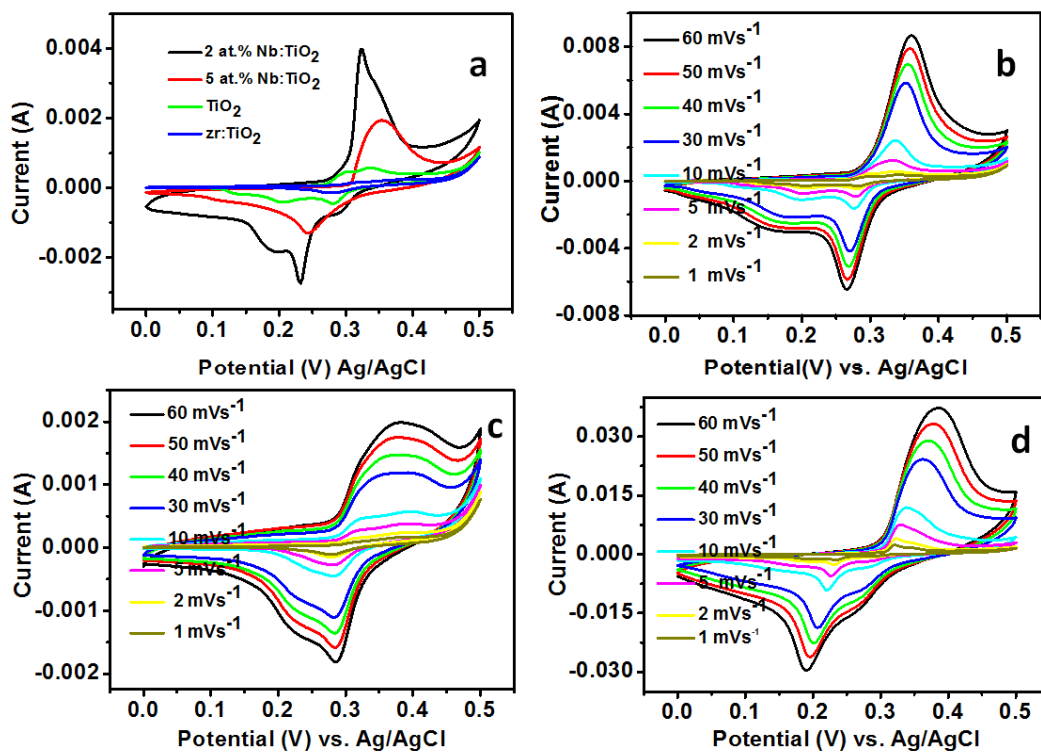
Vidyadharan et.al, Figure: 1



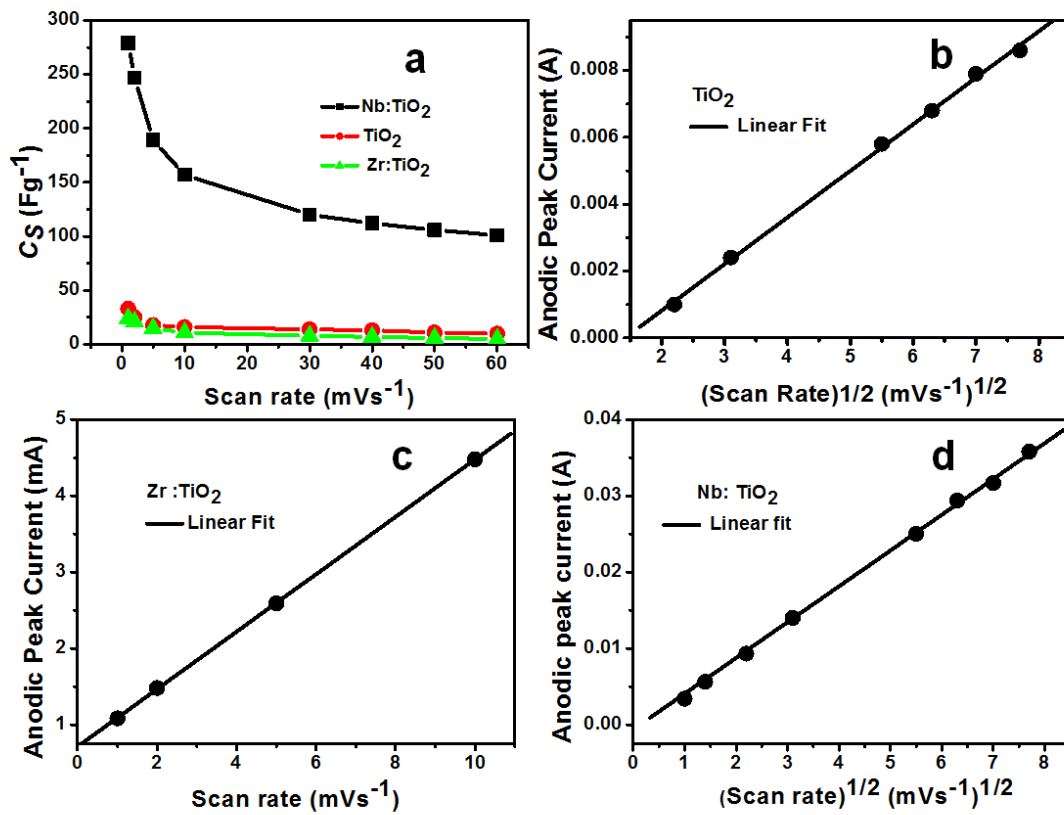
Vidyadharan et.al, Figure: 2



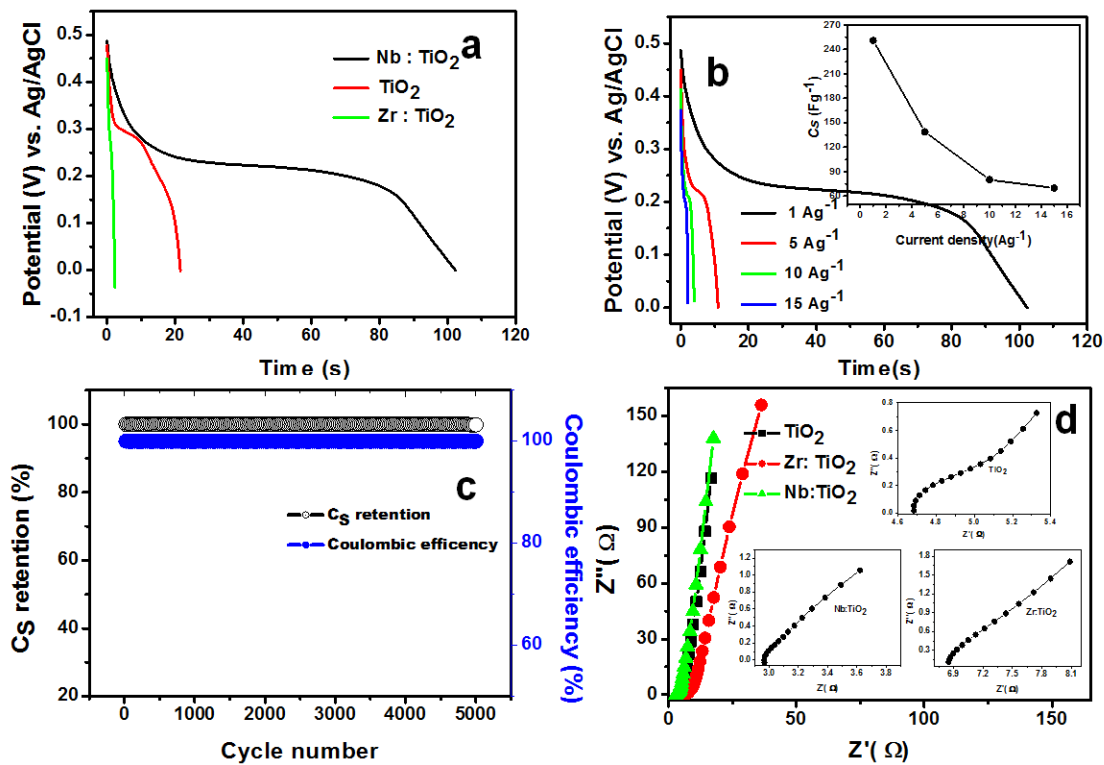
Vidyadharan et.al, Figure: 3



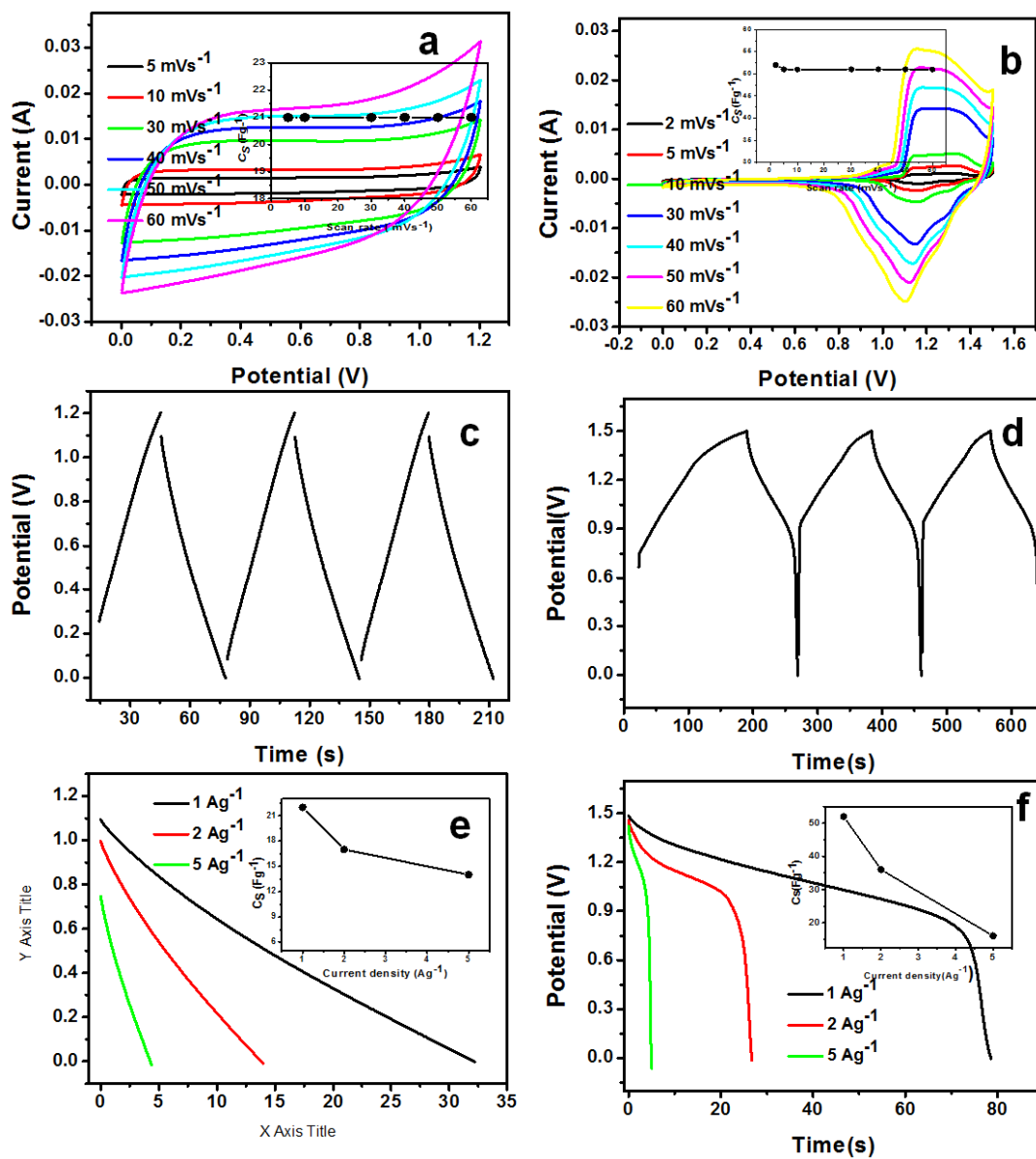
Vidyadharan et.al, Figure: 4



Vidyadharan et.al, Figure: 5



Vidyadharan et.al, Figure: 6



Vidyadharan et.al, Figure: 7

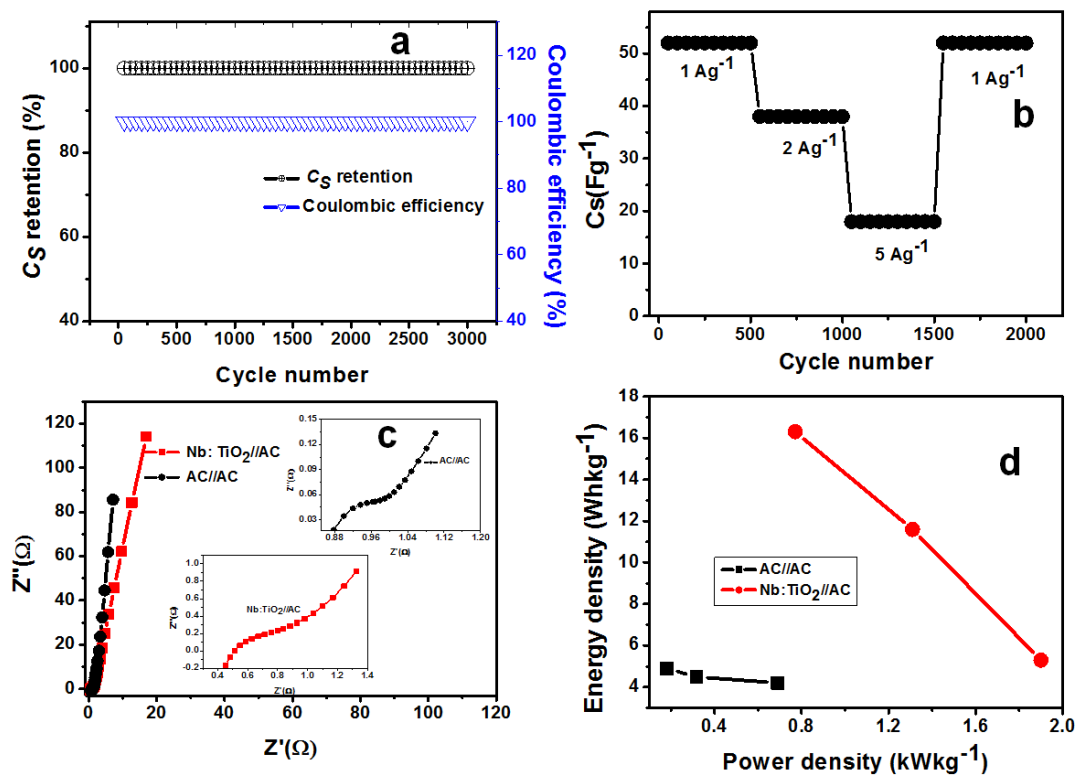
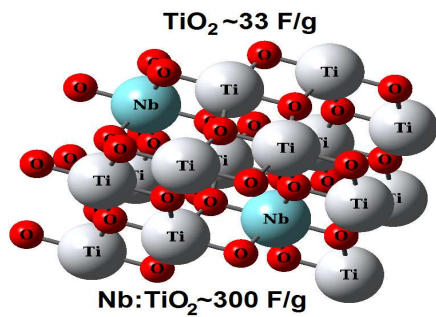


Table of Content



Niobium doped titania nanowires showed an order of magnitude higher capacitance than the parent material